

# Catalysis Science & Technology

Accepted Manuscript



This is an *Accepted Manuscript*, which has been through the Royal Society of Chemistry peer review process and has been accepted for publication.

*Accepted Manuscripts* are published online shortly after acceptance, before technical editing, formatting and proof reading. Using this free service, authors can make their results available to the community, in citable form, before we publish the edited article. We will replace this *Accepted Manuscript* with the edited and formatted *Advance Article* as soon as it is available.

You can find more information about *Accepted Manuscripts* in the [Information for Authors](#).

Please note that technical editing may introduce minor changes to the text and/or graphics, which may alter content. The journal's standard [Terms & Conditions](#) and the [Ethical guidelines](#) still apply. In no event shall the Royal Society of Chemistry be held responsible for any errors or omissions in this *Accepted Manuscript* or any consequences arising from the use of any information it contains.

**Phosphorus-Doped Ordered Mesoporous Carbons embedded with Pd/Fe Bimetal Nanoparticles for the dechlorination of 2,4-dichlorophenol**

Yaoyu Zhou <sup>ab</sup>, Lin Tang<sup>\*ab</sup>, Guide Yang <sup>ab</sup>, Guangming Zeng<sup>\*ab</sup>, Yaocheng Deng <sup>ab</sup>, Bingbing Huang <sup>ab</sup>, Ye Cai <sup>ab</sup>, Jing Tang <sup>ab</sup>, Jingjing Wang <sup>ab</sup>, Yanan Wu <sup>ab</sup>

a College of Environmental Science and Engineering, Hunan University, Changsha, 410082, China,

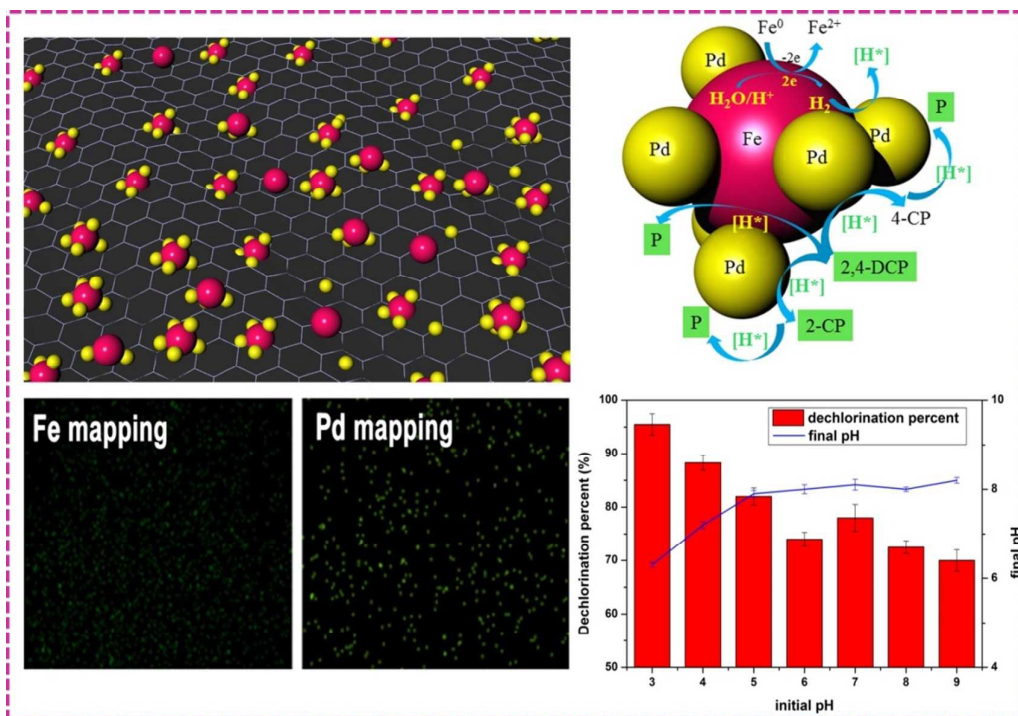
b Key Laboratory of Environmental Biology and Pollution Control (Hunan University), Ministry of Education, Changsha 410082, Hunan, PR China.

---

\*Corresponding author: Tel.: +86-731-88822778; Fax.: +86-731-88822778

E-mail: [tanglin@hnu.edu.cn](mailto:tanglin@hnu.edu.cn)(L. Tang), [zgming@hnu.edu.cn](mailto:zgming@hnu.edu.cn)(G.M. Zeng).

## Graphic abstract



**1 Abstract**

2 Palladium/iron (Pd/Fe) bimetallic nanoparticles was embedded within phosphorus-doped ordered  
3 mesoporous carbons (Pd/NZVI@P) with high dechlorination activity for 2,4-dichlorophenol  
4 (2,4-DCP). The Pd/Fe bimetal nanoparticles with about 15 nm diameter embedded in  
5 phosphorus-doped ordered mesoporous carbons (P-OMC) were homogeneously distributed. The  
6 high dechlorination activity was mainly attributed to the homogeneous distribution of Pd/Fe bimetal  
7 nanoparticles, which was characterized by transmission electron microscopy (TEM) and scanning  
8 electron microscopy/energy dispersive X-ray spectrometry (SEM/EDS) with image mapping.  
9 Dechlorination kinetics indicated that the dechlorination rates of 2,4-DCP increased with the  
10 increasing of Pd content. The use of P-OMC as supporting materials to embed enough Pd/Fe  
11 bimetal nanoparticles kept the nanoparticles highly active and stable. Besides, solution pH had a  
12 significant effect on the dechlorination of 2,4-DCP and the passivation of the Pd/NZVI@P samples.  
13 Effects of the number and position of chlorine atoms for different chlorophenols (CPs) on the  
14 dechlorination activity were also revealed, the result indicated that the dechlorination of CPs by  
15 catalytic reduction preferentially begin from the para-position of the ring, and more chlorine atoms  
16 of CPs are favorable to the occurrence of dechlorination reaction. This study demonstrated that  
17 P-OMC was a promising supporting material to prepare some effective composite metals for the  
18 catalytic dechlorination of CPs.

19

## 20 Introduction

21 Chlorophenols (CPs) are important chemical raw materials and intermediates, and known to be  
22 very toxic even at low concentrations.<sup>1,2</sup> Recently, the synthesis and use of bimetallic materials have  
23 been documented to work efficiently for the dechlorination of chlorophenols (CPs) contaminants.<sup>3-7</sup>  
24 In these bimetallic materials, the first metal (such as Fe, Mg, Al, Zn, Sn, Si) with low standard redox  
25 potential is oxidized more rapidly when coupled with the second metal (Cu, Ni, Ag, or Pd) with high  
26 standard redox potential.<sup>7</sup> Among them, Pd/Fe is the most investigated bimetallic material because  
27 of the excellent hydrogenation activity of Pd and low cost of Fe.<sup>5,8</sup> The high reactivity of nanoscale  
28 Fe/Pd bimetallic material seems promising in liquid phase treatment of CPs, with many reports  
29 focusing on reaction mechanisms, contaminant degradation kinetics, and reaction products.

30 However, some scientific and technical challenges remain in degradation of chlorophenols (CPs)  
31 using Pd/Fe bimetallic material. For example, Pd/Fe bimetallic material have extremely low  
32 solubility in water (at most, 4–5 mg/L),<sup>9,10</sup> and nanoscale Pd and Fe particles are thermodynamically  
33 unstable in solution and tend to aggregate into larger particles.<sup>11,12</sup> Consequently, a stabilizer or a  
34 supporting template is often required to acquire stable and discrete Pd and Fe particles. To achieve  
35 these goals, nanostructured porous carbon materials, such as zeolite,<sup>13</sup> mesoporous silica,<sup>14</sup> active  
36 carbon,<sup>15</sup> mesoporous carbon and multi-walled carbon nanotubes,<sup>16</sup> have been developed for the  
37 popular catalytic supports. Among them, ordered mesoporous carbon (OMC) has obtained great  
38 attention since they were discovered in 1999.<sup>17</sup>

39 Recently, more and more OMC materials were introduced as catalyst supports by researchers for  
40 the reasons as follows: (1) its large surface area and accessible porosity are indispensable when  
41 acquiring a highly dispersed metal nanoparticles on the active nucleation sites of OMC, such as  
42 Pt/carbon,<sup>18</sup> PtCu/carbon,<sup>19</sup> Pd/carbon<sup>20</sup> and PtRu/carbon;<sup>21</sup> (2) the surface and physicochemical

43 properties of OMC can be easily modified with functional groups or incorporated with heteroatoms  
44 (N, B, and S), exhibiting improved physical or chemical properties. Different from the traditional  
45 carbons (including carbon black, activated carbon, carbon nanofibers, and carbon nanotubes) poor in  
46 functional groups, its impregnation of noble metal will not result in aggregation or leaching of the  
47 particles in the liquid solution because of the strong interaction between noble metal and OMC  
48 support. For example, Yu and co-workers reported ordered uniform porous carbon networks with  
49 high surface area and well-developed porosity which were applied to support Pt(50)-Ru(50), and  
50 exhibited much higher specific activity for methanol oxidation than the vulcan carbon-supported  
51 catalyst by about 15%.<sup>22</sup> In our previous studies, magnetic mesoporous carbon incorporated with  
52 polyaniline,<sup>23</sup> iron doped ordered mesoporous carbon<sup>24</sup> and nitrogen-functionalized magnetic  
53 ordered mesoporous carbon<sup>25</sup> were prepared and applied for the removal of pollutants such as  
54 hexavalent chromium, lead and phenol. Zhu and co-workers<sup>26</sup> have successfully prepared magnetic  
55 ordered mesoporous carbon as a catalyst support with superparamagnetic Fe-Pt nanoparticles  
56 without aggregation and particle growth. Zheng et al.<sup>27</sup> reported Pd supported on boron-doped  
57 mesoporous carbon as highly active catalyst for liquid phase catalytic hydrodechlorination. Wang et  
58 al.<sup>28</sup> found Pd and Rh catalysts supported on N-doped mesoporous carbon having higher activities in  
59 the oxidation of benzyl alcohol than other carbon supports.

60 In addition to N and B, phosphorus (P) is expected to fit well into the carbon matrix due to the  
61 P-doping induces defects in the carbon framework and increases the electron delocalization which  
62 promotes active sites.<sup>29</sup> Besides, phosphorus is similar with other heteroatoms (N, B, and S) when  
63 doping in carbon supports, it is also favorable for enhanced metal-support interaction between  
64 superficial metal clusters and substitutional heteroatoms defects,<sup>27,30,31</sup> which may eventually affect  
65 the physicochemical properties of superficial metal particles such as their dispersion and

66 composition. Therefore, it is hypothesized that Pd/Fe bimetallic nanoparticles embedded within  
67 innovative phosphorus-doped ordered mesoporous carbons would display unique catalytic  
68 performance.

69 Herein, we employed a series of phosphorus-doped ordered mesoporous carbons (P-OMC)  
70 composites incorporated with reactive Fe and Pd bimetallic nanoparticles (Pd/NZVI@P) as effective  
71 and stable catalyst for the dechlorination of CPs in wastewater. Fe particles was in-situ formed and  
72 incorporated in the P-OMC with uniform distribution, small size and high surface to increase their  
73 mechanical activity and stability, and noble metal Pd was applied to modify Fe surface to facilitate  
74 electron generation for CPs dechlorination. In this work, 2,4-dichlorophenol was selected as a  
75 model pollutant to evaluate the dechlorination activity. The effect of Pd loadings on the  
76 hydrodechlorination of 2,4-dichlorophenol was investigated. Moreover, as known, the passivation  
77 of Fe-based materials significantly affects the dechlorination of CPs. Though some experimental  
78 parameters, such as solution temperature and initial substrate concentration, as well as the reaction  
79 pathway of nanoscale Pd-Fe for dechlorination have been previously investigated in literature,<sup>8</sup> the  
80 underlying mechanism for the passivation and the effect of solution pH on the passivation and  
81 activity have not yet been clearly elucidated. In this work, the effect of solution pH on the  
82 dechlorination and passivation of the Pd/NZVI@P was studied carefully, and the possible reasons  
83 were revealed.

## 84 **Experimental**

### 85 **Chemicals and materials**

86 Pluronic copolymer P123 (EO<sub>20</sub>PO<sub>70</sub>EO<sub>20</sub>, EO=ethylene oxide, PO=propylene oxide) and  
87 triphenylphosphine (TPP) were purchased from Sigma-Aldrich (USA). All reagents were

88 analytical-grade and used as received without further purification. High-purity water (18.2 MΩ/cm)  
89 from a Millipore Milli-Q water purification system was used in each experiment.

### 90 **Synthesis of Pd/NZVI@P catalysts**

91 The mesoporous template SBA-15 was prepared according to our previous study (As presented in  
92 supporting information).<sup>32-35</sup> The preparation of P-OMC nanoparticles used conventional ordered  
93 mesoporous silica SBA-15 with rodlike shape as a hard template. The carbon replica is then  
94 prepared by infiltrating the mesopores of 1000 mg SBA-15 with 400 mg triphenylphosphine (TPP)  
95 in 10 mL of ethyl alcohol at room temperature. And then, 2.0 mL furfuryl alcohol was added  
96 dropwise into the above mixture. After that, the mixture thus prepared was heated at 80 °C for 10 h  
97 in air and calcinated at 900 °C for 2 h under flowing nitrogen atmosphere. After dissolving the  
98 silica framework with 2.0 mol/L NaOH solution at 90 °C, the resultant solid was filtered, washed,  
99 dried and then stored in a nitrogen-filled glovebox until required. Details about the preparation of  
100 Pd/NZVI@P-0%, Pd/NZVI@P-0.5%, Pd/NZVI@P-1% and Pd/NZVI@P-2% are presented in  
101 Supporting Information (SI). For the purpose of comparisons, Pd/NZVI/OMC was also prepared by  
102 the similar method.

### 103 **Characterization**

104 Transmission electron microscopy (TEM, JEOL JEM-1230), high-resolution TEM (HR-TEM) at  
105 an accelerating voltage of 200 KV and Scanning electron microscope (SEM, JEOL JSM-6700)  
106 images were used to investigate the morphology and structure of Pd/NZVI@P. X-ray diffraction  
107 (Rigaku D/max-II B) was applied to analyze the composite materials. The Energy dispersive X-ray  
108 (EDX) analysis in the SEM image was applied to detect the element mapping of the Pd/NZVI@P.  
109 Nitrogen adsorption measurements at 77 K were performed using an ASAP 2020 volumetric  
110 adsorption analyzer. Raman spectroscopy was mounted by using a LabRam HR800 Raman

111 spectrometry. Thermo gravimetric–differential thermal analysis (DTG–DTA) was completed in  
112 order to determine relevant phase transition temperatures. X–ray photoelectron spectroscopy (XPS,  
113 Thermo Fisher Scientific, UK) was recorded to analyze the surface elemental composition.

### 114 **Dechlorination Experiments**

115 All dechlorination experiments were carried out in 50 mL flasks containing 50 mg/L 2,4–DCP  
116 solution and a certain amount of Pd/NZVI@P, and the flasks were shaken at 150 rpm in a shaker at  
117 25 °C. Before each experiment, 5 mg of Pd/NZVI@P–2% nanoparticles was added in 2,4–DCP  
118 solution at initial pH 3.0, and the residual 2,4–DCP concentration was measured at 150 min. In  
119 comparison of different CPs dechlorination, 5 mg of Pd/NZVI@P–2% were placed in solutions of  
120 2–CP, 4–CP, 2,4–DCP and 2,4,6–TCP at initial pH 3.0, and the reaction time was 150 min. In the  
121 investigation of initial pH effect on the dechlorination, 5 mg of Pd/NZVI@P–2% were added in  
122 2,4–DCP solution at pH from 3.0 to 9.0 (pH were adjusted by adding dilute oxalic acid solution or  
123 aqueous ammonia), and 2,4–DCP concentration and pH in solution were measured during 150 min.  
124 All batch systems were carried out in conical flasks with ground–in glass stoppers, and the reaction  
125 solution was deoxygenated by inert gas. Each experiment was conducted in triplicate, and the  
126 standard deviations were calculated.

### 127 **2,4–dichlorophenol Analysis**

128 After the dechlorination experiments, the solid was separated from the solution by a filter with a  
129 0.45 µm membrane filter, and the residual 2,4–DCP concentration in solution was measured by  
130 HPLC. The analytical parameters, the equation for dechlorination percents, and pseudo–first–order  
131 kinetic model were described in Supporting Information.

## 132 **Results and discussion**

### 133 **Catalysts Characterization**

134 The formation of highly ordered uniform pore distribution can be seen in the TEM images of  
135 SBA-15 and P-OMC in Fig. 1a and Fig. 1b, demonstrating that the resultant mesoporous materials  
136 possess well ordered 2D hexagonal mesostructures. The TEM and SEM of Pd/NZVI@P were  
137 presented in Fig. 1c and Fig. 1d, respectively. As seen in Fig. 1c, the black nanoparticles dispersed  
138 uniformly on the P-OMC were Pd/Fe bimetal nanoparticles, and the nanoparticles with an average  
139 diameter about 15 nm were dispersed on the carbon matrix. SEM image revealed that the  
140 mesoporous sample consisted of many rope-like domains with relatively uniform lengths, which  
141 were aggregated into wheat-like macrostructures (Fig. 1d). Pd/Fe bimetal nanoparticles particles  
142 dispersed on the P-OMC. In addition, as seen in Fig. S-1 and Fig. S-2, it is clearly to observe that  
143 Pd/Fe bimetallic nanoparticles supported on OMC with P results in smaller and higher dispersion  
144 particles compared to without P. Furthermore, SEM can give an elemental distribution map through  
145 images of back-scattered electron and EDS as well as surface topographic information through those  
146 of secondary electrons.<sup>11,36</sup> Fig. 2 shows SEM photograph and the corresponding EDS elemental  
147 mapping of Pd/NZVI@P-2%. The EDS elemental maps confirm that C, P, Fe and Pd elements are  
148 highly dispersed in Pd/NZVI@P. The relative atomic contents of these elements are listed in Table  
149 S-1.

150 **“Here Fig.1”**

151 **“Here Fig.2”**

152 The N<sub>2</sub> adsorption-desorption isotherms and Barrett-Joyner-Halenda (BJH) mesopore size  
153 distribution plots of SBA-15, P-OMC, Pd/NZVI@P-0%, Pd/NZVI@P-0.5%, Pd/NZVI@P-1% and  
154 Pd/NZVI@P-2% were presented in Fig. 3. Their corresponding Brunauer-Emmett-Teller (BET)  
155 surface area, pore volume, pore diameter are summarized in Table S-2. All samples show  
156 representative type-IV curves with H2 hysteresis loops (Fig. 3A), reflecting the uniform pore size

157 distributions of the mesopores before and after P, Fe and Pd-incorporation with SBA-15. And the  
158 pore size distribution curves calculated from desorption branches clearly confirm their narrow pore  
159 size distribution. Compared with SBA-15, P-OMC revealed a slight change in the H<sub>2</sub> hysteresis  
160 loop, demonstrating that P was introduced into the carbon materials. The corresponding pore size  
161 distributions calculated from the adsorption branch clearly confirmed that (Fig. S3b) the pore sizes  
162 of SBA-15 were centered at around 10 nm. In contrast, the adsorption pore size distribution of  
163 P-OMC was centered at 5 nm. The difference could be attributed either to the shrinkage of filled  
164 carbon phosphide polymeric material inside the pores of SBA-15 during the high temperature  
165 treatment of the mesoporous silica/carbon phosphide composite or to the partial filling of the CN  
166 matrix in the mesopores of SBA-15. The introduction of P led to a distinct increase in  
167 Brunauer–Emmett–Teller (BET) surface areas (from 473.897 to 1033.5 m<sup>2</sup>·g<sup>-1</sup>) and pore volume  
168 (from 1.134 to 1.446 cm<sup>3</sup>·g<sup>-1</sup>). These might be due to P entering into channels occupying partial  
169 space of pores. The BET surface area of P-OMC is 1033.5 m<sup>2</sup>·g<sup>-1</sup>. Interestingly, upon doping Fe  
170 and different Pd bulk into P-OMC, the BET surface areas of Pd/NZVI@P-0% (only Fe doped into  
171 P-OMC), Pd/NZVI@P-0.5%, Pd/NZVI@P-1% and Pd/NZVI@P-2% are 667.746, 552.42, 455.53  
172 and 344.22 m<sup>2</sup>·g<sup>-1</sup>, respectively (Table S-2). The mean pore sizes of Pd/NZVI@P-0%,  
173 Pd/NZVI@P-0.5%, Pd/NZVI@P-1% and Pd/NZVI@P-2% are 5.087, 5.058, 5.011 and 4.979 nm,  
174 respectively (Table S-2). The specific surface area and pore volumes of the samples increased  
175 obviously, and decrease slightly after the supporting of the Fe and Pd (Table S-2), suggesting that  
176 there existed some smaller Pd/Fe particles inside the pore framework which occupied partial space  
177 of the pore canals. Compared with P-OMC, there is only slight change on the mesoporous size of  
178 P-OMC with the Pd/Fe bimetal nanoparticles embedded, suggesting that the ordered mesostructure  
179 is still well-preserved after immobilization of Fe and Pd, which are beneficial to the catalyst.

180

**“Here Fig.3”**

181 The small-angle X-ray diffraction (SAXRD) patterns of composite materials are presented in Fig.  
182 4. Usually, SAXRD reveals whether the formation of ordered mesostructure was changed during the  
183 preparation of materials. For the composite materials, the XRD patterns show three well-resolved  
184 peaks (the (100), (110) and (200) peaks) with a hexagonal mesopore arrangement at  $2\theta$  of about  
185  $0.89^\circ$ ,  $1.55^\circ$ , and  $1.88^\circ$ , which illustrates the framework hexagonal ordering of ordered mesoporous  
186 structure is basically retained in the process of material preparation, and also indicates a high  
187 periodic order in the arrangement of symmetry cells, which is in agreement with the TEM  
188 observations (see Fig. 1). Besides, another phenomenon should be noticed is that the intensity of  
189 diffraction peaks of composites decreases slightly with the introduction of Fe and Pd into P-OMC.  
190 These observations indicate that some of the Pd/Fe nanoparticles are located inside mesoporous  
191 carbon pores while some are located at the orifice of pores.

192

**“Here Fig.4”**

193

**“Here Fig.5”**

194 To elucidate the chemical composition, nature of bonding, and purity of the sample, the structural  
195 properties of the Pd/NZVI@P-2% particle were further investigated by XPS, and their spectra are  
196 shown in Fig. 5a, Fig. 5b and Fig. 5c. As seen in Fig. 5a, Pd/NZVI@P is mainly composed of carbon  
197 (C1s) and oxygen (O1s), with small amounts of phosphorus (P2p), iron (Fe 2p) and palladium  
198 (Pd3d). The presence of phosphorus comes from the pyrolyzation of triphenylphosphine, and iron  
199 and palladium mainly come from the reduction of  $\text{Fe}(\text{NO}_3)_3 \cdot 9\text{H}_2\text{O}$  and palladium chloride inside the  
200 mesopores of P-OMC. Furthermore, the high-resolution P2p XPS spectrum (Fig. 5a inset) reveals  
201 the presence of both P-O bonding ( $134.03 \text{ eV}$ ) and P-C bonding ( $132.41 \text{ eV}$ ) in Pd/NZVI@P  
202 catalyst. The two results strongly suggest that the P atoms are incorporated into the carbon

203 framework of the P-OMCs. In addition, the peaks at 134.03 eV and 132.41 eV are positively shifted  
204 3.63 eV and 2.01 eV compared with that of pure P (130.4 eV). The positive shift of the P2p peak  
205 indicates that there is a strong interaction between P, C and O.<sup>37</sup>

206 The Pd 3d regions of the particle are shown in Fig. 5b. For the Pd/NZVI@P-2%, the main doublet  
207 at 335.41 eV (Pd<sup>0</sup>) and 336.48 eV (Pd<sup>2+</sup>) are the characteristic of metallic Pd, this suggests that both  
208 Pd<sup>0</sup> and Pd<sup>2+</sup> coexist on the Pd/NZVI@P-2%, and the content of Pd<sup>0</sup> (68.22%) is larger than Pd<sup>2+</sup>  
209 (61.78%). XPS analysis was also used to study the variation of the Fe oxidation state in resultant  
210 Pd/NZVI@P catalysts. As shown in Figure 5c, the Fe 2p photoelectron spectrum of Pd/NZVI@P-2%  
211 showed four peaks around 725.11, 717.43, 712.36 and 706.26 eV in the Fe2p<sub>1/2</sub>, Satellite Fe<sup>3+</sup>,  
212 Fe2p<sub>3/2</sub> and Fe<sup>0</sup>, clearly indicating the Fe<sup>0</sup> species in the resultant of Pd/NZVI@P catalysts. The  
213 results further confirm the Pd<sup>0</sup> and Fe<sup>0</sup> are incorporated into the carbon framework of the P-OMCs,  
214 which was also proved by previous SAXRD analysis.

215 Raman spectra illustrate the D-band and G-band of nanocomposites, giving some additional  
216 information of the carbon lattice. As seen in Fig. 5d, the nanocomposites possess both D mode peak  
217 and G mode peak, which are near 1363 cm<sup>-1</sup> and 1577 cm<sup>-1</sup>, respectively. D mode is corresponding  
218 to the disordered sp<sup>2</sup>-hybridized carbon atoms, while G mode is related to the structural integrity of  
219 sp<sup>2</sup>-hybridized carbon atoms of ordered mesoporous carbons.<sup>38</sup> The ratio between the disorder and  
220 graphite area bands (I<sub>D</sub>/I<sub>G</sub>) is interpreted as a measure of the degree of the material's orderliness and  
221 graphitization. As shown in Fig. 5d, the I<sub>D</sub>/I<sub>G</sub> ratio of P-OMC, Pd/NZVI@P-0%,  
222 Pd/NZVI@P-0.5%, Pd/NZVI@P-1% and Pd/NZVI@P-2% was 0.954, 0.922, 0.911, 0.901 and  
223 0.894, respectively. The result indicating that the incorporation of Fe and Pd led to the tiny  
224 graphitization of Pd/NZVI@P. Besides, thermo gravimetric-differential thermal analysis

225 (DTG–DTA) was also used to characterize the catalysts (Fig. S–3), and the description was  
226 presented in Supporting Information.

### 227 **Activity of Pd/NZVI@P on Removal of 2,4–dichlorophenol**

228 The dechlorination activity of the Pd/NZVI@P was investigated. As seen in Fig. 6, the  
229 concentration of 2–CP was higher than that of 4–CP in the process of reaction, suggesting that the  
230 chlorine in para–position is easier to be expelled, which is in agreement with the previous  
231 publications other cases that dechlorination of chlorophenols by catalytic reduction method began  
232 from the para–position of the ring.<sup>39,40</sup>

233 Interestingly, the phenol species could be detected as soon as the reaction occurred, and this  
234 phenomenon was also reported by Wei et al.<sup>8</sup> We assumed that the 2,4–DCP species were partly  
235 transformed into phenol directly prior to the appearance of transitional products. Moreover, it can be  
236 seen that 2,4–DCP concentration decreased while 2–CP, 4–CP and phenol (P) concentration  
237 increased with increasing reaction time to 150 min, and the total concentrations of phenolics  
238 (2,4–DCP, 2–CP, 4–CP and phenol) in solution were similar to the initial 2,4–DCP concentration,  
239 indicating that 2,4–DCP was directly reduced to 2,4–DCP, 2–CP, 4–CP and phenol in this process,  
240 and their amounts adsorbed on the bimetal were negligible. Given these observations, the hypothesis  
241 for the possible dechlorination processes was accordingly presented in Fig. 7.

242 **“Here Fig.6”**

243 **“Here Fig.7”**

244 During the catalytic hydrodechlorination of 2,4–dichlorophenol by Pd/NZVI@P, the factors  
245 including Pd content may have important effect on the characteristics of the Pd/NZVI@P and the  
246 dechlorination activity. Fig.8 shows the dechlorination of 2,4–DCP on the Pd/NZVI@P prepared  
247 with different Pd amounts. The pseudo–first–order rate constants ( $k_{\text{obs}}$ ) increased with increasing Pd

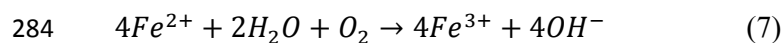
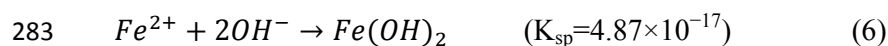
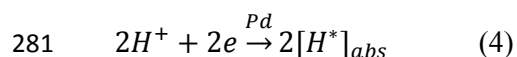
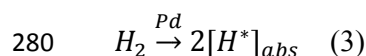
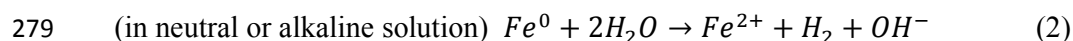
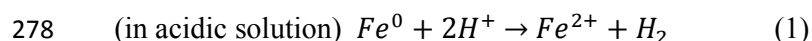
248 content, similar to the trend of dechlorination efficiency. The Pd/NZVI@P with high Pd content  
249 displayed remarkable dechlorination activity, while the pure iron exhibited very poor dechlorination  
250 activity (Fig. 8). The Pd/NZVI@P can form some galvanic cells, and Fe passed electrons to the  
251 catalytic Pd, which played an important roles in both the acceleration of Fe corrosion and  
252 enhancement of dechlorination activity.<sup>7</sup> The low dechlorination efficiency over the pure Fe particles  
253 demonstrated that direct dechlorination of 2,4-DCP was difficult to occur without the assistance of  
254 Pd. The addition of Pd significantly improved the dechlorination of 2,4-DCP due to the mechanism  
255 of catalytic hydrodechlorination. The Pd/NZVI@P-2% was adopted in the following experiments.  
256 The batch experimental results indicated that the 2,4-DCP species in aqueous solution were  
257 dechlorinated by Pd/NZVI@P-2%, followed by the formation and transformation of intermediate  
258 products 2-CP and 4-CP, eventually with the final product of phenol. Besides, the dechlorination of  
259 2,4-dichlorophenol by Pd/NZVI/OMC-2% and Pd/NZVI@P-2% was also compared, and the result  
260 was presented in Fig. S-4, it's clear that P-OMC is more suitable as a support to be embedded with  
261 Pd/Fe bimetal nanoparticles for the dechlorination of 2,4-dichlorophenol, which is probably  
262 ascribed to the incorporation of heteroatoms (P).

263 **“Here Fig.8”**

#### 264 **Effect of pH on Dechlorination and Passivation**

265 To investigate the pH effect on the dechlorination and passivation of the Pd/NZVI@P, the  
266 dechlorination of 2,4-DCP at different initial pH were studied. As shown in Fig. 9, we found that the  
267 dechlorination efficiency of 2,4-DCP decreased when the initial pH increased from 3.0 to 6.0 (in  
268 acidic solution). However, when the initial pH was adjusted to 7.0, the dechlorination efficiency  
269 improved slightly, and then decreased from 7.0 to 9.0 (in alkaline solution). Besides, it is clearly  
270 seen that the final pH increased when the initial pH increased from 3.0 to 8.0 during the

271 dechlorination reaction. When the initial pH was 8.0, the final pH after the reaction was still around  
 272 8.0. However, the final pH decreased during the reaction when the initial pH was 9.0, this  
 273 phenomena were also reported in other works.<sup>8</sup> Specifically, the pH variation profile in the reaction  
 274 process was also investigated. The pH value during the dechlorination reaction increased fast within  
 275 the initial 10 min, then gradually reached to the highest value (As shown in Fig. S-3), further  
 276 decreased with increasing time, and finally kept at relatively stable after 90 min. In the initial stage,  
 277 Fe was dissolved in solution and 2,4-DCP was dechlorinated due to the following reactions.<sup>8,41</sup>



286 These reactions caused the change of pH due to the consumption/formation of  $H^+$  or consumption/  
 287 formation of  $OH^-$ , making the solution pH change. As seen from Eq 6, the precipitation of  $Fe(OH)_2$   
 288 occurred when the ion corrosion product of  $Fe^{2+}$  and  $OH^-$  was higher than the solubility product with  
 289 the increase of  $Fe^{2+}$  and  $OH^-$  concentrations. In addition,  $Fe(OH)_3$  can easily form, especially in the  
 290 presence of dissolved oxygen (eqs 7 and 8) though the solubility product of  $Fe(OH)_3$  is much lower  
 291 than that of  $Fe(OH)_2$ . And the solution pH decreased due to the fast consumption of  $OH^-$  via the  
 292 formation of iron hydroxide precipitate (eq 6-8).<sup>42</sup>

293 However, when the initial pH increased from 3.0 to 8.0, the precipitation rate was lower than the  
294 consumption of  $H^+$  or generation rate of  $Fe^{2+}$ , and solution pH still increased until the consumption  
295 of  $H^+$  or generation rate of  $Fe^{2+}$  decreased to its precipitation rate or consumption of  $OH^-$ . When the  
296 initial pH was 8.0, the overall reaction equilibrium of the consumption of  $H^+$  and  $OH^-$  was achieved  
297 at relatively stable pH. Finally, when the initial pH was 9.0, the highest pH values exceeded 8.0 in  
298 the reaction process, accelerating the formation of passive film by iron hydroxide resulting in the  
299 final pH decrease.

300 Besides, on the basis of the reaction mechanisms (eqs 1–8), we could speculate that the main  
301 factors affecting dechlorination efficiency were: (I) the generated rate of  $[H]_{abs}$ , which is related to  
302 the pH and the amount of Pd/NZVI@P (eqs 1–4); (II) the passivation film by iron hydroxide, which  
303 could inhibit the contact of target compounds with the reactive sites and block the electron transfer;  
304 (III) the loss of Fe during reaction, resulting in the slow and even complete stop of dechlorination  
305 reaction. In acidic solution, with the increase of  $H^+$  concentration, the generated rate of  $[H]_{abs}$  will  
306 increase quickly. Although the formation of passivating film is hard due to the fact that the  
307 precipitation rate was lower than the consumption of  $H^+$ , the excessive  $H^+$  can remarkably result in  
308 the loss of Fe. However, the dechlorination efficiency of 2,4–DCP still increased quickly with the  
309 decrease of the initial pH (Fig. 9, the initial pH decreased from 6.0 to 3.0). The reason might be that  
310 despite the increasing  $H^+$  resulted in the loss of Fe, the use of P-OMC as supporting material could  
311 provide enough Pd/Fe bimetal nanoparticles with high activity and stability, and the passivating film  
312 by iron hydroxide could be ignored. Thus, we speculate that the generated rate of  $[H]_{abs}$  is the main  
313 influence on dechlorination efficiency in acidic solution. In alkaline solution, the passivating film is  
314 formed easily, at initial pH beyond 7.0, the highest pH values exceeded 9.0 in the reaction process,  
315 accelerating the formation of passive film by precipitation. Some formed Fe (II) and Fe (III)

316 precipitates covered on the particle surface and retarded Fe dissolution (eqs 2), resulting in the slow  
317 dechlorination. Thus, with the increase of pH, the dechlorination efficiency decreased obviously. We  
318 speculate that the passivating film by iron hydroxide is the main limitation factors on dechlorination  
319 efficiency in alkaline solution. Moreover, it is clearly seen that alkaline solution is unfavorable for  
320 dechlorination compared with acidic solution. It is unexpected that the dechlorination efficiency  
321 improved slightly in neutral solution compared with the initial pH of 6.0. As described previously,  
322 the  $[H]_{\text{abs}}$  in pH of 6.0 is absolutely higher than that in neutral solution, which suppressed the  
323 formation of passivating film by iron hydroxide, which are conducive to the dechlorination. But the  
324 result is just the opposite. Interestingly, when the initial pH were 6.0 and 7.0, after 150 min the final  
325 pH was similarly (see Fig. S-5), indicating that the rate of formation of  $\text{OH}^-$  was faster compared  
326 with the initial pH of 6.0. Thus, we speculate that the initial pH of 6.0 led to formation of more  
327 passivating film compared with that in neutral solution, and this might be the main impact factor on  
328 dechlorination. In addition, the dissolved total iron ions and palladium ions concentrations at  
329 different pH after Pd/NZVI@P reaction with 2,4-DCP in 150 min were also measured. As shown in  
330 Fig. S-6A, after Pd/NZVI@P reaction with 2,4-DCP, Pd/NZVI@P bimetal in acidic conditions  
331 releases iron ions because ZVI can react with  $\text{H}^+$ . The concentration of iron ions decreased with the  
332 increase of pH. However, there were nearly no palladium ions released at pH ranging from 3.0 to 9.0  
333 because palladium just acted as the electronic conduction. As seen in Fig. S-6B, there were nearly  
334 no P released at pH ranging from 3.0 to 9.0 after the reaction, the reason may be that P is not directly  
335 involved in dechlorination of 2,4-dichlorophenol.

336 In general, solution pH not only affects the dechlorination of 2,4-DCP but also influences the  
337 formation of iron hydroxide precipitate and the passivation. Low pH can cause the fast  
338 dechlorination but result in dissolution of bimetal. The increasing pH accelerated the formation of

339 iron precipitates, and passivating film was formed. Therefore, it is crucial to control solution pH in a  
340 reasonable range to balance the dechlorination and passivation of bimetal.

341 **“Here Fig.9”**

### 342 **Effect of the number and Position of Chlorine atoms of CPs on the Dechlorination activity**

343 In addition, we preliminarily discussed the number and position of chlorine atoms on CPs for the  
344 dechlorination activity of the Pd/NZVI@P. In this study, 2-CP, 4-CP, 2,4-DCP and  
345 2,4,6-trichlorophenol (2,4,6-TCP) were used as the substrates. As shown in Fig. 10, the  $K_{obs}$  of  
346 different CPs follow the order of 2,4,6-TCP > 2,4-DCP > 4-CP > 2-CP, and the dechlorination  
347 efficiency obey the same order with  $K_{obs}$  during the dechlorination reaction (0–150 min). The  
348 result further implies that the dechlorination of CPs by chemical reactions preferentially begin from  
349 the para-position of the ring ( $K_{obs}$  (4-CP) >  $K_{obs}$  (2-CP)), and more chlorine atoms of CPs are  
350 favorable to take place the C-Cl bond cleavage reaction. This phenomenon was also reported by  
351 other works.<sup>38,39,43</sup>

352 **“Here Fig.10”**

### 353 **Conclusions**

354 The Pd/Fe bimetal nanoparticles embedded within phosphorus-doped ordered mesoporous carbons  
355 (Pd/NZVI@P) had high catalytic dechlorination activity for 2,4-DCP. In acidic, neutral or alkaline  
356 solution conditions, Pd/NZVI@P can completely remove 2,4-DCP from wastewater. Besides, the  
357 main factors affecting dechlorination efficiency related to solution pH were revealed. The high and  
358 stable dechlorination of 2,4-DCP was attributed to the homogeneous distribution of Pd/Fe bimetal  
359 nanoparticles into phosphorus-doped ordered mesoporous carbons phase. This study demonstrated  
360 that P-OMC was a promising supporting material to prepare some effective composite metals for

361 the catalytic dechlorination of CPs. Many bimetallic materials may also be supported by P-OMC  
362 with great prospects for wastewater treatment to dechlorinate CPs.

### 363 **Supporting Information**

364 More details about the preparation of SBA-15 templates, 2,4-dichlorophenol analysis and thermo  
365 gravimetric-differential thermal analysis. This material is available free of charge via the Internet at  
366 <http://pubs.acs.org>.

### 367 **ACKNOWLEDGMENTS**

368 The study was financially supported by the National Program for Support of Top-Notch Young  
369 Professionals of China (2012), Projects 51222805, 51579096, 51521006 and 51508175 supported by  
370 National Natural Science Foundation of China, the Program for New Century Excellent Talents in  
371 University from the Ministry of Education of China (NCET-11-0129), Interdisciplinary Research  
372 Project of Hunan University, the Fundamental Research Funds for the Central Universities, Hunan  
373 University, the Hunan Province Innovation Foundation for Postgraduate (no. CX2015B095).

### 374 **REFERENCES**

- 375 1. J. Xu, Q. Jiang, T. Chen, F. Wu, Y. X. Li, *Catal. Sci. Technol.*, 2015, **5**, 1504-1513.
- 376 2. L. Yin, Z. Shen, J. Niu, J. Chen, Y. Duan, *Environ. Sci. Technol.*, 2010, **44**, 9117-9122.
- 377 3. S. Agarwal, S. R. Al-Abed, D. D. Dionysiou, *Environ. Sci. Technol.*, 2007, **41**, 3722-3727.
- 378 4. U. D. Patel, S. Suresh, *J Hazard Mater.*, 2008, **156**, 308-316.
- 379 5. Y. Weile, A. A. Herzing, L. X. Qin, C. J. Kiely, Z. W. Xian, *Environ. Sci. Technol.*, 2010, **44**,  
380 4288-4294.
- 381 6. R. Devor, K. Carvalho-Knighton, B. Aitken, P. Maloney, E. Holland, L. Talalaj, R. Fidler, S.  
382 Elsheimer, C. A. Clausen. C. L. Geiger, *Chemosphere*, 2009, **76**, 761-766.
- 383 7. F. Xu, S. Deng, J. Xu, W. Zhang, M. Wu, B. Wang, J. Huang, G. Yu, *Environ. Sci. Technol.*,  
384 2012, **46**, 4576-4582.
- 385 8. J. Wei, X. Xu, Y. Liu, D. Wang, *Water. Res.*, 2006, **40**, 348-354.
- 386 9. R. G. Luthy, G. R. Aiken, M. L. Brusseau, S. D. Cunningham, P. M. Gschwend, J. J.  
387 Pignatello, M. Reinhard, S. J. Traina, W. J. Weber, J. C. Westall, *Environ. Sci. Technol.*, 1997, **31**,  
388 3341-3347.
- 389 10. N. Saleh, K. Sirk, Y. Liu, T. Phenrat, B. Dufour, K. Matyjaszewski, R. D. Tilton, G. V.  
390 Lowry, *Environ. Eng. Sci.*, 2007, **24**, 45-57.
- 391 11. Y. Wang, H. Zhao, G. Zhao, *Appl. Catal., B* 2015, **164**, 396-406.
- 392 12. M. Zhang, D. B. Bacik, C. B. Roberts, D. Zhao, *Water. Res.*, 2013, **47**, 3706-3715.
- 393 13. S. Navalon, M. Alvaro, H. Garcia, *Cheminform*, 2010, **99**, 1-26.

- 394 14. M. Hartmann, S. Kullmann, H. Keller, *J. Mater. Chem.*, 2010, **20**, 9002-9017
- 395 15. S. Navalon, A. Dhakshinamoorthy, M. Alvaro, H. Garcia, *Chemsuschem*, 2011, **4**,
- 396 1712-1730.
- 397 16. C. Z. Yuan, L. Chen, B. Gao, L. H. Su, Q. X. Zhang, *J. Mater. Chem.*, 2009, **19**, 246-252.
- 398 17. R. Ryoo, H. J. Sang, S. Jun, *J. Phys. Chem B.*, 1999, **37**, 7743-7746.
- 399 18. F. B. Su, Z. Q. Tian, C. K. Poh, Z. Wang, S. H. Lim, Z. L. Liu, *Chem Mater.*, 2010, **22**, 832.
- 400 19. G. Gupta, D. A. Slanac, P. Kumar, J. D. Wiggins-Camacho, X. Wang, S. Swinnea, K. L.
- 401 More, S. Dai, K. J. Stevenson, K. P. Johnston, *Chem Mater.*, 2009, **21**, 4515-4526.
- 402 20. Z. Li, J. Liu, Z. Huang, Y. Yang, C. Xia, F. Li, *ACS Catal.*, 2013, **3**, 839-845.
- 403 21. Z. Liu, F. Su, X. Zhang, S. W. Tay, *ACS Appl. Mater. Interfaces.*, 2011, **3**, 3824-3830.
- 404 22. J. S. Yu, S. Kang, S. B. Yoon, G. Chai, *J. Am. Chem. Soc.*, 2002, **124**, 9382-9383.
- 405 23. G. Yang, L. Tang, Y. Cai, G. Zeng, P. Guo, G. Chen, Y. Zhou, J. Tang, J. Chen, W. Xiong,
- 406 *Rsc Advances*, 2014, **4**, 58362-5871.
- 407 24 T. Lin, G. D. Yang, G. M. Zeng, C. Ye, S. S. Li, Y. Y. Zhou, Y. Pang, Y. Y. Liu, Y. Zhang.
- 408 *Chem. Eng. J.*, 2014, **239**, 114-122.
- 409 25. G. Yang, T. Lin, G. Zeng, C. Ye, T. Jing, Y. Pang, Y. Zhou, Y. Liu, J. Wang, S. Zhang.
- 410 *Chem. Eng. J.*, 2015, **259**, 854-864.
- 411 26. Y. Zhu, E. Kockrick, S. Kaskel, T. Ikoma, N. Hanagata, *J J. Phys. Chem C.*, 2009, **113**,
- 412 5998-6002.
- 413 27. J. Zhou, W. Ke, W. Wang, Z. Xu, H. Wan, S. Zheng, *Appl. Catal., A* 2014, **470**, 336-343.
- 414 28. B. Wang, M. Lin, T.P. Ang, J. Chang, Y.H. Yang, A. Borgna, *Catal Commun.*, 2012, **25**, 96–
- 415 101
- 416 29. D.S. Yang, D. Bhattacharjya, S. Inamdar, J. Park, J.S. Yu, *J. Am. Chem. Soc.*, 2012, **134**,
- 417 16127–16130.
- 418 30. C.K. Acharya, C.H. Turner, *J. Phys. Chem B.*, 2006, **110**, 17706–17710.
- 419 31. C.K. Acharya, C.H. Turner, *J. Phys. Chem C.*, 2007, **111**, 14804–14812.
- 420 32. L. Tang, Y. Zhou, G. Zeng, Z. Li, Y. Liu, Y. Zhang, G. Chen, G. Yang, X. Lei, M. Wu,
- 421 *Analyst*, 2013, **138**, 3552-3560.
- 422 33. Y. Zhou, L. Tang, G. Zeng, J. Chen, J. Wang, C. Fan, G. Yang, Y. Zhang, X. Xie, *Biosens.*
- 423 *Bioelectron.*, 2015, **65**, 382-389.
- 424 34. Y. Zhou, L. Tang, G. Zeng, J. Chen, Y. Cai, Y. Zhang, G. Yang, Y. Liu, C. Zhang, W. Tang,
- 425 *Biosens. Bioelectron.*, 2014, **61**, 519-525.35.
- 426 35. J. X. Liu, W. J. Zhou, J. L. Gong, L. Tang, Y. Zhang, H. Y. Yu, B. Wang, X. M. Xu, G. M.
- 427 Zeng, *Bioresource Technol.*, 2008, **18**, 8748-8751.
- 428 36. S. Wang, Q. Zhao, H. Wei, J. Q. Wang, M. Cho, H. S. Cho, O. Terasaki, Y. Wan, *J. Am.*
- 429 *Chem. Soc.*, 2013, **135**, 11849-11860.
- 430 37. L. X. Ding, A. L. Wang, G. R. Li, Z. Q. Liu, W. X. Zhao, C. Y. Su, Y. X. Tong, *J. Am. Chem.*
- 431 *Soc.*, 2012, **134**, 5730-5733.
- 432 38. S. Shrestha, S. Asheghi, J. Timbro, W. E. Mustain, *Carbon*, 2013, **60**, 28-40.
- 433 39. K. C. Christoforidis, M. Louloudi, Y. Deligiannakis, *Appl. Catal. B.*, 2010, **95**, 297-302.
- 434 40. G. Díaz-Díaz, M. Celis-García, M. C. Blanco-López, M. J. Lobo-Castañón, A. J.
- 435 Miranda-Ordieres, P. Tuñón-Blanco, *Appl. Catal. B.*, 2010, **96**, 51-56.
- 436 41. X. Wang, M. Zhu, H. Liu, J. Ma, F. Li, *Sci Total Environ.*, 2013, **449**, 157-167.
- 437 42. C. C. Liu, D. H. Tseng, C. Wang, *J. Hazard. Mater.*, 2006, **136**, 706-713.
- 438 43. S. Agarwal, S. R. Al-Abed, D. D. Dionysiou, E. Graybill, *Environ. Sci. Technol.*, 2008, **43**,
- 439 915-921.

### Figure Captions

**Figure 1:** TEM images of SBA-15 (a), P-OMC (b) and Pd/NZVI@P-2% (c), SEM of Pd/NZVI@P-2% (d).

**Figure 2:** SEM photograph and elemental mapping images of Pd/NZVI@P-2% for C, P, Fe and Pd.

**Figure 3:** Nitrogen sorption isotherms (a) of nanocomposites and the corresponding pore size distribution curves of composite materials.

**Figure 4:** Small-angle X-ray diffraction (SAXRD) patterns of nanocomposites.

**Figure 5:** XPS wide-scan spectrum of the Pd/NZVI@P-1% nanocatalyst (a), the XPS spectrum of the spent Pd 3d (b) and Fe 2p (c) catalyst, respectively. Raman spectra (d) of nanocomposites.

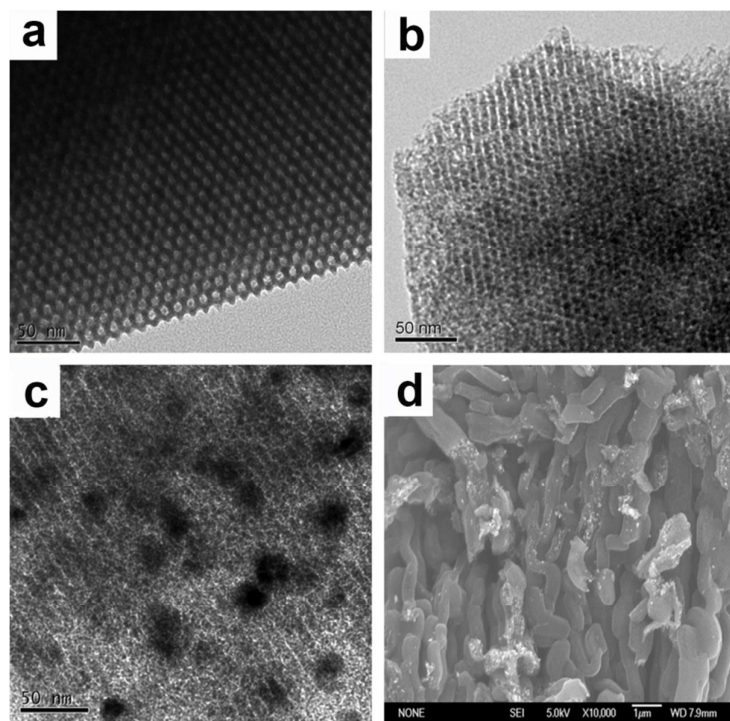
**Figure 6:** Transformation of 2,4-dichlorophenol by 5 mg nanoscale Pd/NZVI@P-2%,  $C_0=50$  mg/L,  $T=25$  °C, pH=3.

**Figure 7:** The hypothesis for the possible dechlorination processes of 2,4-DCP.

**Figure 8:** Effect of Pd bulk loading on removal ratio of 2,4-dichlorophenol.

**Figure 9:** Effect of initial pH and final pH on the dechlorination kinetics of 2,4-dichlorophenol.

**Figure 10:** The dechlorination activity of the Pd/NZVI@P-2% for different CPs (5 mg nanoscale Pd/NZVI@P-2%,  $C_0=50$  mg/L,  $T=25$  °C, pH=3).

**Fig.1**

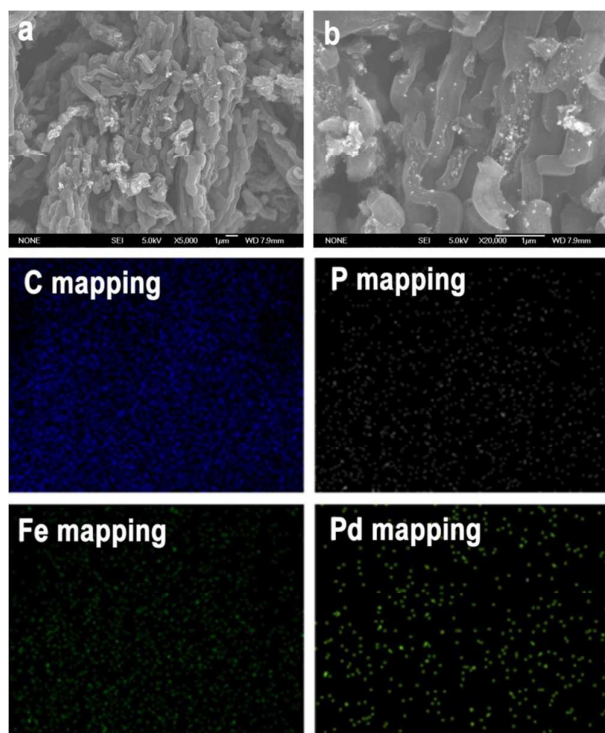


Fig.2

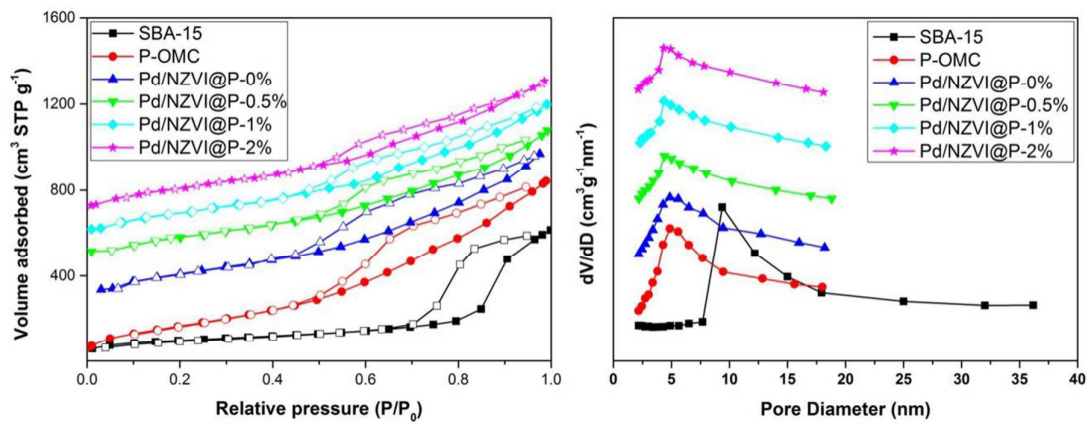


Fig.3

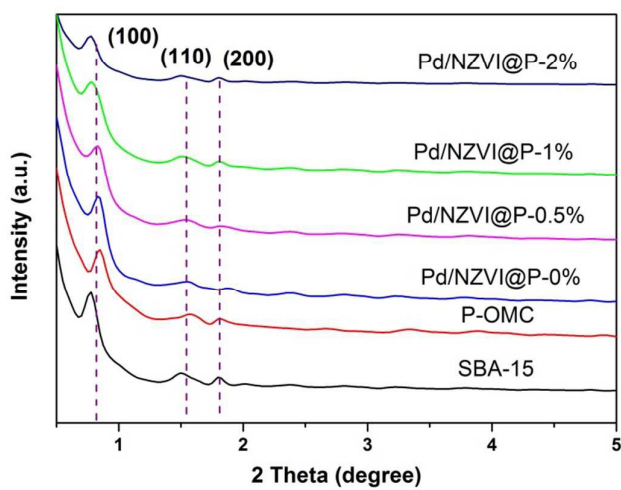


Fig.4

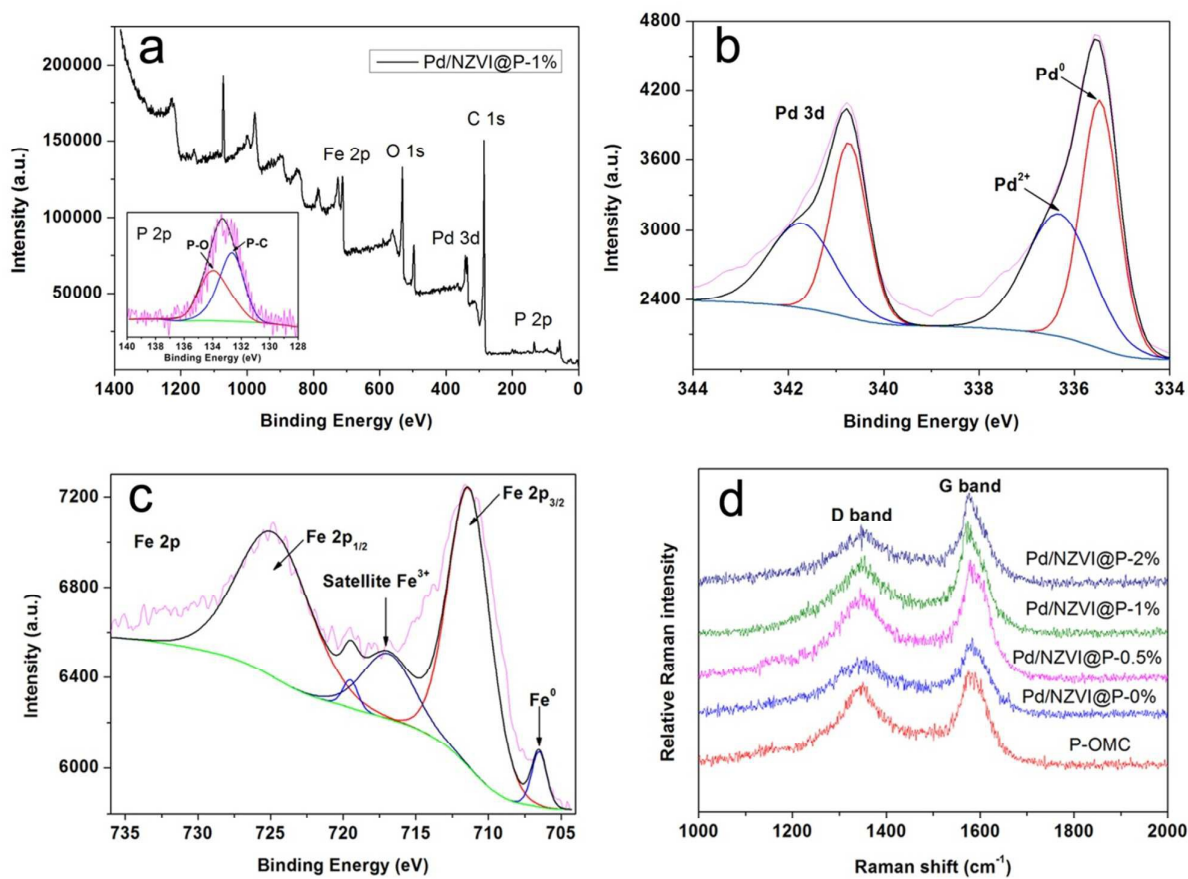


Fig.5

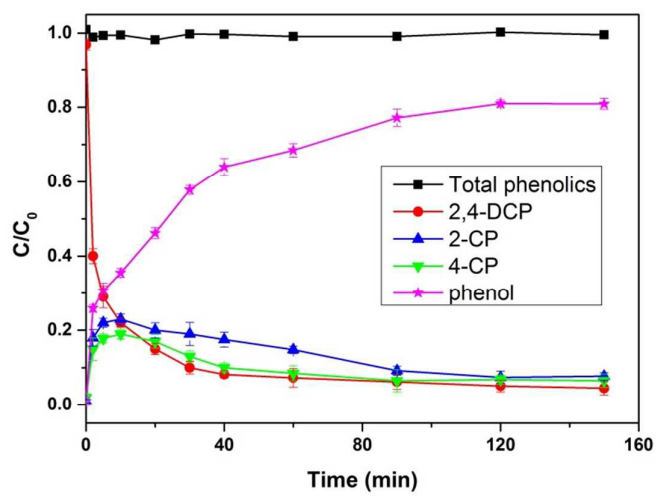


Fig.6

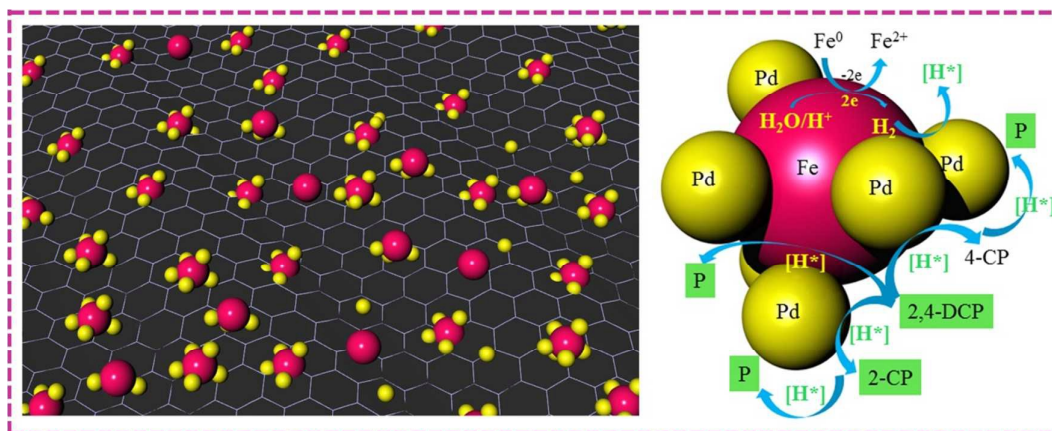


Fig.7

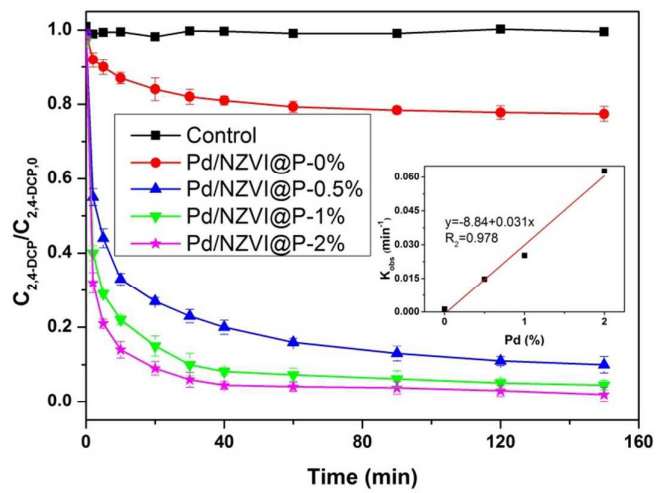


Fig.8

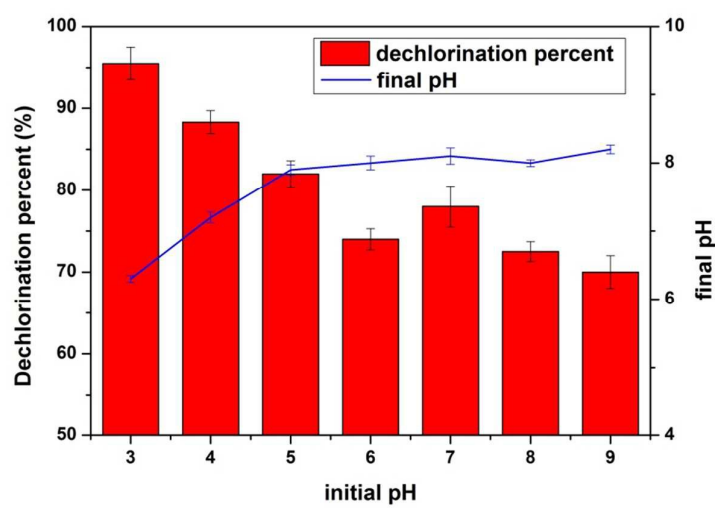


Fig.9

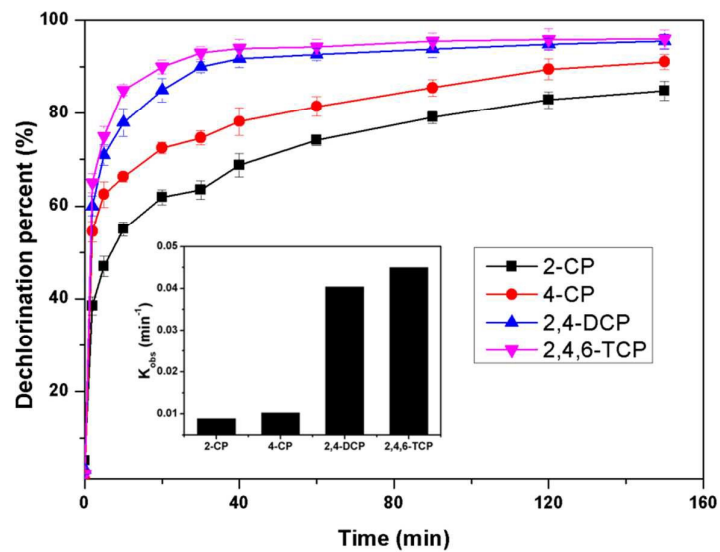
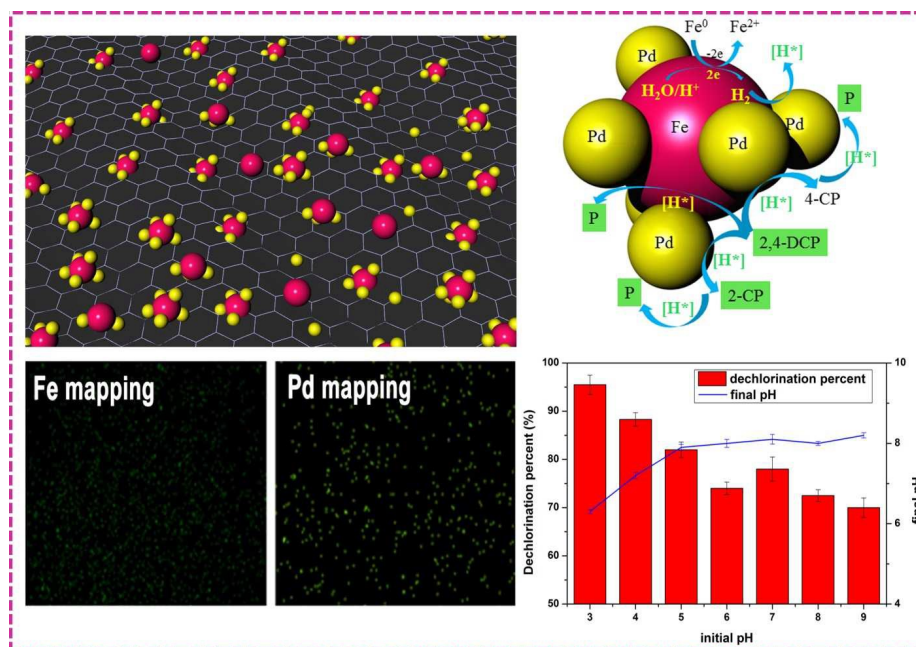


Fig.10



Pd-Fe bimetal nanoparticles embedded within phosphorus-doped ordered mesoporous carbons as highly active and stable catalyst for the degradation of 2,4-dichlorophenol